Dopant Selection Strategy for High Quality Factor Localized Surface Plasmon Resonance from Doped Metal Oxide Nanocrystals

Bharat Tandon[†‡], Sandeep Ghosh[†], Delia J. Milliron[†]*

[†]*McKetta Department of Chemical Engineering, University of Texas at Austin, Austin, Texas 78712-1589, United States*

[‡]*Department of Chemistry, Indian Institute of Science Education and Research, Dr. Homi Bhabha Road, Pune-411008, India*

Supporting Information

Contents

Text S1: Nanocrystal Synthesis

Chemicals: All chemicals used in the synthesis and characterization of nanocrystals were acquired commercially and no further purification step was carried out prior to their use. Indium(III) acetate (STREM, ≥99.99%) zirconium(IV) acetylacetonate (Sigma-Aldrich, 97%), tin(IV) acetate (Sigma-Aldrich 99.99%), oleyl alcohol (Sigma-Aldrich, 85%) and oleic acid (Sigma-Aldrich, 90%) were used for the synthesis. Oleylamine (Sigma-Aldrich, 70%), ethanol (Fischer Chemical, 90%), hexane (Fischer Chemical ≥99.9%) and tetrachloroethylene (Sigma-Aldrich, ≥99.9%) were utilized for washing the resulting nanocrystals and characterizing them through different techniques.

Synthesis Procedure:

Different Zr-doped, Sn-doped, and Sn-Zr codoped In_2O_3 NCs were synthesized by minor modifications of the slow-injection synthetic procedure developed by the Hutchison group.[1] Using standard Schlenk line techniques, a 0.5 M mixture of In and Zr precursors in 10 mL oleic acid was degassed at 100 ˚C under vacuum conditions, which was followed by an undisturbed heating and vigorous stirring at 150˚C under N_2 atmosphere for 2 hours. 8 mL of this mixture was subsequently injected into an already degassed 13 mL solution of oleyl alcohol kept at 290˚C (under N_2 conditions) at the rate of 0.2 mL/min using a syringe pump. Nanocrystals were separated from the reaction mixture impurities by repeatedly precipitating with ethanol, centrifugation at 9000 rpm for 5 min, and re-dispersing in hexane before finally being prepared as a colloidal dispersion of NCs in hexane. The same synthesis protocol was followed for Sn-doped In_2O_3 NCs (Sn:In_2O_3) and Sn-Zr codoped In_2O_3 (Sn,Zr:In_2O_3) NCs. The synthetic yield of all reactions lied in the 65-80% range.

For different Zr doping percentages, the amount of Zr and In precursor was varied accordingly. It is customary to note here that the incorporation of Zr in In_2O_3 has been found to be difficult under the aforementioned experimental conditions. With the slow-injection synthesis strategy adopted here, Zr doping efficiency was limited at approximately 25%. Therefore, to synthesize 1.3% Zr-doped In_2O_3 (Zr:In_2O_3) NCs, 0.25 mmol of $Zr(acac)_4$ was mixed with 4.75 mmol of $In(ac)_3$ in 10 mL oleic acid. Similar calculations can be performed for other Zr doping percentages in both

Zr:In_2O_3 NCs and Sn,Zr:In_2O_3 NCs while keeping in consideration that irrespective of the target composition, the total metal concentration in the solution should be 0.5 M.

Text S2: Nanocrystal Characterization

X-ray diffraction (XRD): For determining the crystal structure and phase purity using XRD, as-synthesized NCs were drop-casted on a small piece of Si wafer. Powder XRD patterns were then obtained through a Rigaku Miniflex 600 instrument operating in a Bragg-Brentano geometry with Cu Kα (λ = 1.5406 Å) as the X-ray source. The same samples were also used in for X-ray photoelectron spectroscopy.

Raman Spectroscopy: Presence of an amorphous ZrO_2/In_2O_3 phase and other impurities undetected in powder- XRD was checked via a Horiba LabRAM Aramis instrument equipped with confocal aperture. Samples were prepared by drop-casting a solution of Zr:In_2O_3 NCs on 2x2 glass slide followed by air-drying. All Raman spectra were obtained with a ×50 microscope objective at an excitation wavelength of 532 nm and an acquisition time of 180 s.

Transmission electron microscopy (TEM): Size and morphology of the NCs were examined using a low-resolution scanning TEM (STEM). Sample preparation for STEM involved drop-casting and subsequently air-drying 20 μL dilute solution of NCs in hexane (~15 mg/mL of NCs in 1 mL hexane) on copper TEM grid. STEM micrographs were obtained on a Hitachi S5500 operating at an accelerating voltage of 30 mV in the STEM mode. The average diameter and standard deviation in sizes of different NCs were obtained by analyzing 100 particles from their respective STEM images using ImageJ software and fitting the statistics to a Gaussian size distribution. High-resolution TEM (HRTEM) images of the same NCs were obtained on a JEOL 2010F TEM operating at 200 kV accelerating voltage.

Inductively coupled plasma-optical emission spectroscopy (ICP-OES): Doping percentages of Zr or Sn in In_2O_3 were experimentally attained by employing ICP-OES technique on a Varian 720-ES ICP Optical Emission Spectrometer. Samples for the ICP-OES were prepared by digesting 1-2 mg of the powder NCs in aqua-regia solution (a mixture of 35% concentrated HCl and 70% HNO_3 in 3:1 ratio respectively) for 24 hours. This was followed by diluting the acid solution with milli-Q water such that the total acid concentration becomes approximately 2% v/v. Standard

solutions of variable concentration for different elements were prepared by diluting the commercial ICP-OES standard with 2% HNO_3 solution in milli-Q water.

X-ray photoelectron spectroscopy (XPS): To develop an understanding about the oxidation state of different elements and their doping percentages within the NCs, XPS spectra of different NCs were recorded on a Kratos X-ray Photoelectron Spectrometer – Axis Ultra DLD using a monochromatic Al Kα radiation (λ = 1486.6 eV) and a charge neutralizer. The XPS spectra obtained for different elements were carbon corrected by fixing the adventitious C1s peak to 284.8 eV binding energy and analyzed through CasaXPS software. Doping percentages for Zr and/or Sn were calculated by taking a ratio of the integrated area under the Zr 3d peak and/or Sn 3d peak with that under the In 3d, Zr 3d and Sn 3d XPS peaks while taking into consideration the sensitivity factors of the different elements involved.

Optical Spectroscopy: The absorption spectra of different NCs, which helped us to analyze the LSPR of different Zr:In_2O_3 NCs were collected through Fourier transform infrared (FTIR) liquid cell in a Bruker Vertex 70 FTIR. The dispersion of NCs in tetrachloroethylene was injected through a syringe in the liquid cell between two infrared transparent KBr windows separated by a path length of 0.5 mm. For highly doped Sn:In_2O_3 NCs and Sn,Zr:In_2O_3 NCs, near-infrared spectra were recorded in Agilent Cary 5000 spectrophotometer using a quartz cuvette with a path length of 10 mm.

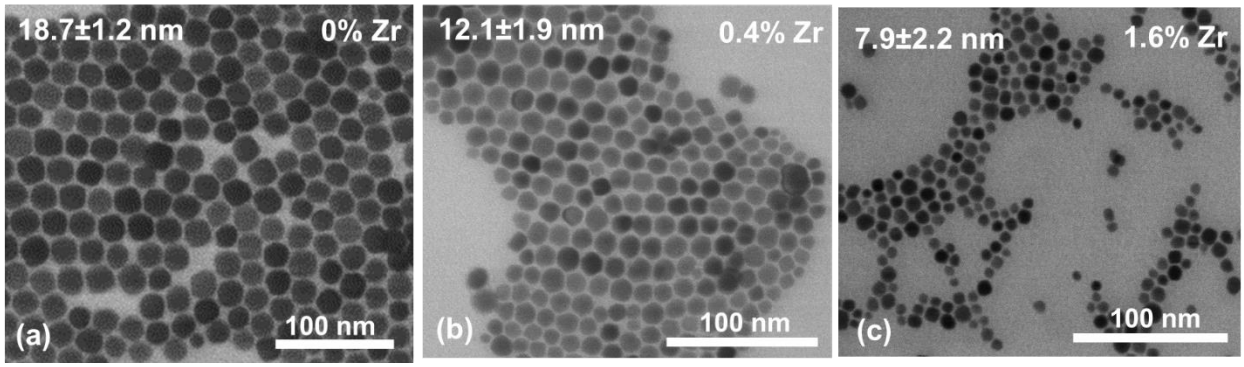

Figure S1: STEM images for different Zr:In_2O_3 NCs.

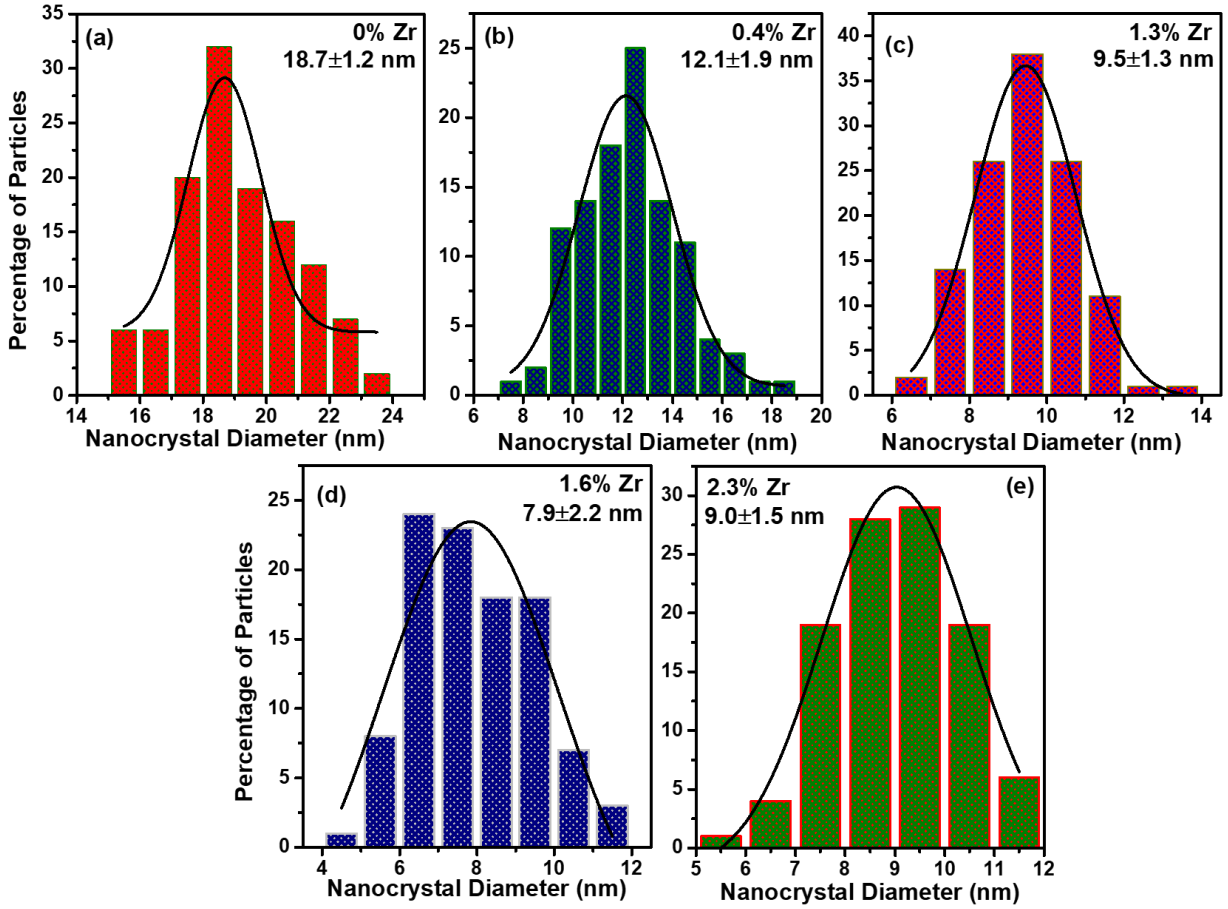

Figure S2: Size distribution plots of different Zr:In_2O_3 NCs obtained by analyzing particles from their representative STEM images in Figure 1c-d and Figure S1.

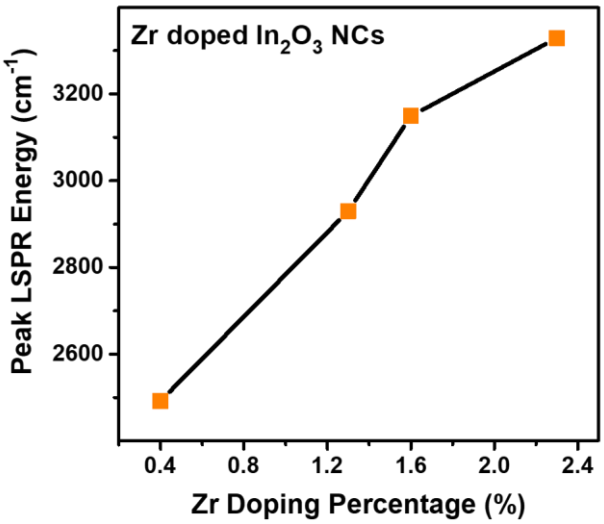

Figure S3: Variation in the peak LSPR energy of Zr:In_2O_3 NCs with an increase in the Zr doping percentage.

Table ST1: Tabulated experimental LSPR parameters of different NCs obtained from their optical extinction spectra.

Composition	**LSPR Peak Energy (cm^{-1})**	**LSPR FWHM (cm^{-1})**	**LSPR Q-Factor**
0% Doping	1296	648	2.0
0.4% Zr	2492	870	2.9
1.3% Zr	2930	735	4.0
1.6% Zr	3149	936	3.4
2.3% Zr	3329	840	4.0
0.6% Sn	2001	1038	1.9
2.8% Sn	4058	1188	3.4
4.1% Sn	4732	1274	3.7
7.5% Sn	5695	1204	4.7
1.9% Sn-0.9% Zr	3652	696	5.3
0.9% Sn-0.4% Zr	3026	860	3.5
4.5% Sn-0.8% Zr	4838	1071	4.6
7.5% Sn-1.0% Zr	5531	1066	5.3

Table ST2: Comparison of the LSPR parameters and Q-factors of Zr:In_2O_3 and Sn,Zr:In_2O_3 NCs with the benchmark materials for near and mid-infrared LSPR in the literature.

Host	Dopant	Doping Level (%)	LSPR Peak (cm^{-1})	FWHM (meV)	Q-factor	Reference Number
CdO	F^- , In^{3+}	~10, 8.3	5793	59	12.23	2
CdO	In^{3+}	13.2	4415	67	8.15	3
In_2O_3	Sn^{4+}, Cr^{3+}	6.6, 23.8	5717	99	7.2	4
In_2O_3	Zr^{4+}, Sn^{4+}	0.9, 1.9	3652	86	5.3	Present case
In_2O_3	Zr^{4+}, Sn^{4+}	1.0, 7.5	5531	132	5.3	Present case
In_2O_3	Sn^{4+}	6.4	5882	~150	4.85	5
In_2O_3	Zr^{4+}	1.3	2930	91	4.0	Present case
In_2O_3	Zr^{4+}	2.3	3329	104	4.0	Present case
In_2O_3	Ce^{4+}	5.2	2522	77	4.08	6
ZnO	Al^{3+}	1.6	~2500	~100	3.9*	7
$Cu_{2-x}S$	Cu vacancy	~3	5564	210	3.3	8
WO_{3-x}	O vacancy	~5%	~11700	~900	1.6	9
ZnO	Ga^{3+}	~2.5	~1667	-	<1.0	10
TiO_2	Nb^{5+}	15.9	~4000	>450	~1	11

* = Result obtained from single nanocrystal spectroscopy

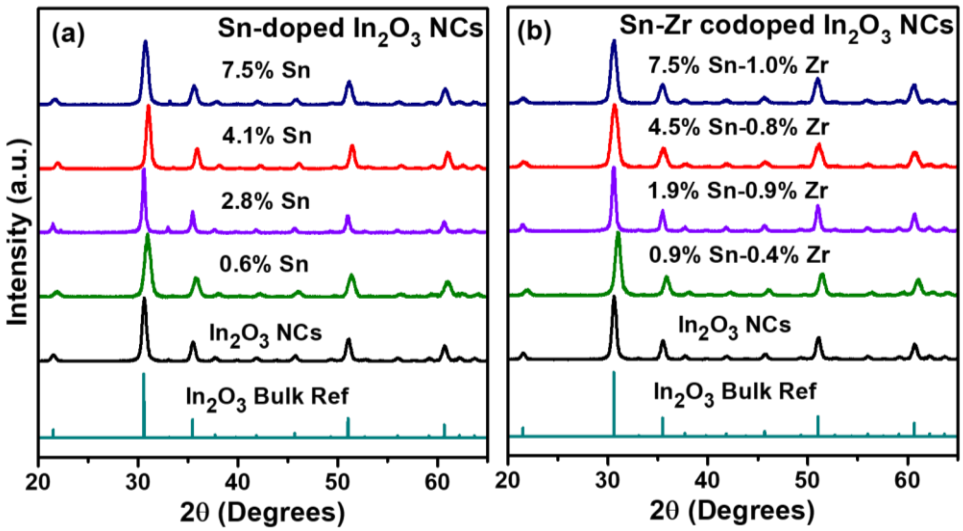

Figure S4: XRD patterns of (a) Sn:In_2O_3 and, (b) Sn,Zr:In_2O_3 NCs with reference to the bulk In_2O_3 reference (JCPDS 88-2160) showing the absence of any impurity phase and retention of the cubic bixbyite structure.

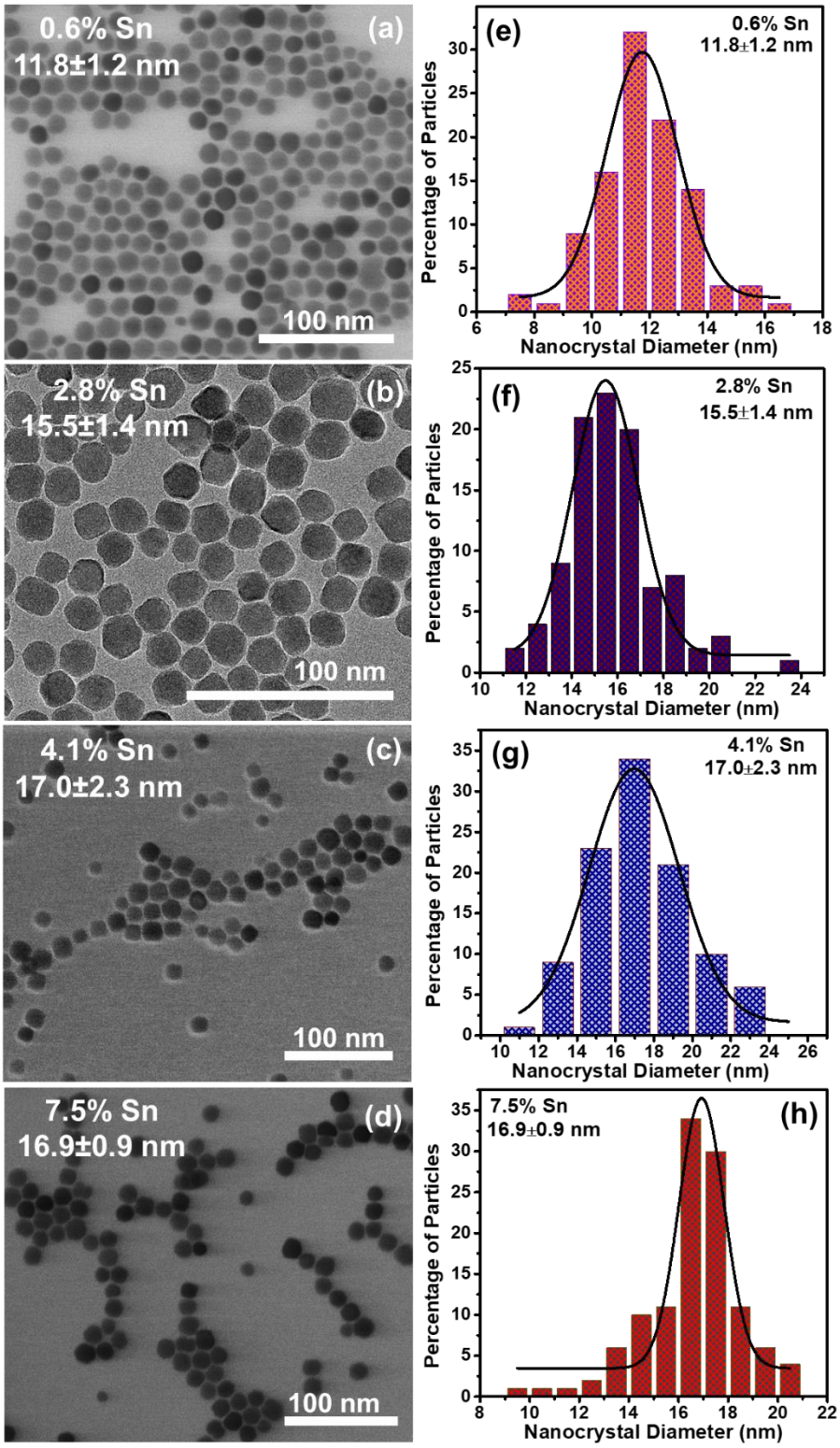

Figure S5: STEM images and size distribution curves (obtained by analyzing the diameter of particles) for Sn:In_2O_3 NCs with different Sn doping percentages.

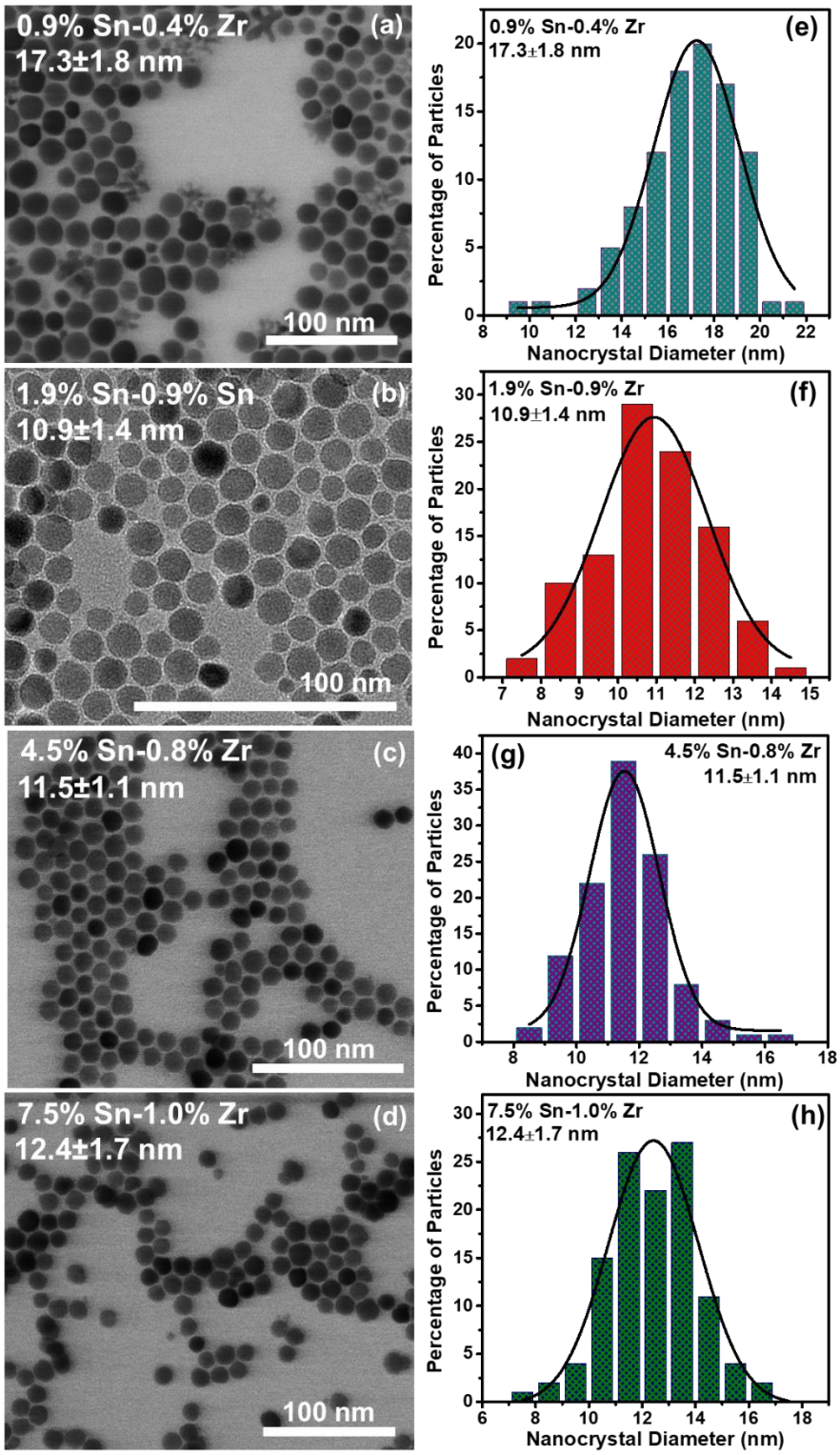

Figure S6: STEM images and size distribution curves (obtained by analyzing the diameter of particles) for Sn,Zr:In_2O_3 NCs with different Sn doping percentages but an almost constant (~1%) Zr doping percentage.

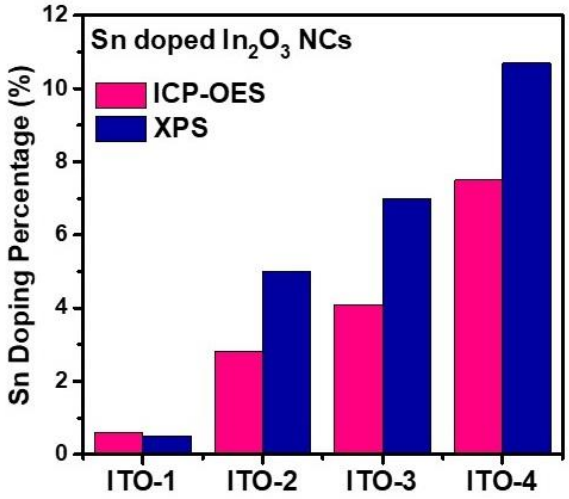

Figure S7: Correlation between the XPS and ICP-OES doping percentages of different Sn:In_2O_3 NCs establishing that the radial distribution of Sn is slightly surface segregated. The notations ITO-1 to ITO-4 on the x-axis just represents NCs with 4 different Sn doping percentages.

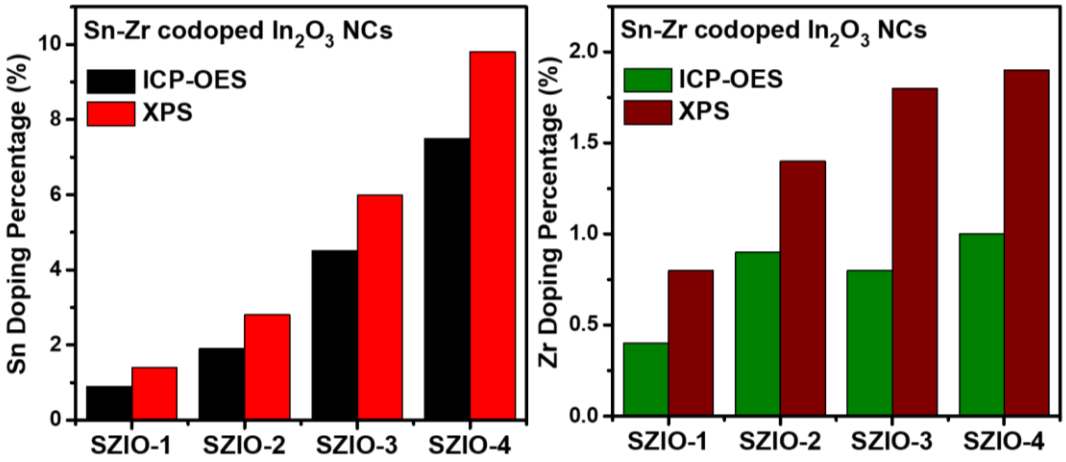

Figure S8: Correlation between the XPS and ICP-OES doping percentages of different Sn,Zr:In_2O_3 NCs establishing that the radial distribution of Sn, (a) is slightly surface segregated whereas that of Zr, (b) is highly surface segregated. The notations SZIO-1 to SZIO-4 on the x-axis just represents NCs with 4 different compositions of Sn,Zr codoped In_2O_3 NCs.

Text S3: Simple Drude and extended Drude modeling of the optical extinction spectra

The electric field of the incoming electromagnetic radiation interacts with the total electron density present in the material, in a form of light-matter interaction. The essence of polarization of conduction and valence band electrons by the external electric field is recorded by the complex

dielectric function, which ultimately governs the optical properties of the material. Since LSPR derives only from conduction band electrons (free electrons), the frequency-dependent complex dielectric function ε_D can be defined just by the contribution of free electrons, given by the simple Drude model

$$\varepsilon_D(\omega) = \varepsilon_\infty - \frac{\omega_p^2}{\omega^2 + i\omega\Gamma} \qquad (1)$$

Where ε_∞ is the high-frequency dielectric constant for the material (taken as 3.9 for all NCs), ω_P is the bulk plasma frequency given by equation (2) and Γ is the frequency-independent damping constant.

$$\omega_p^2 = \frac{ne^2}{\varepsilon_0 m^*} \qquad (2)$$

here, n is the free carrier density in the material (per cm^{-3}), e is the electronic charge, ε_0 is the dielectric permittivity of vacuum, and m^* is the effective mass of the carriers.

However, the simple Drude model is valid only when the damping of charge carriers occurs by a frequency-independent mechanism such as electron-electron scattering, electron-photon scattering, surface scattering, or phonon-phonon scattering as in noble metal NCs. In doped semiconductors it is often necessary to also consider ionized impurity scattering where the electric field experienced by the charge carrier is much different above and below the bulk plasma frequency.[12, 13]

To take into account the frequency-dependent scattering of charge carriers, an extended Drude model is employed where the essence of frequency-dependent carrier scattering is considered through an empirical equation

$$\Gamma(\omega) = \Gamma_L - \frac{\Gamma_L - \Gamma_H}{\pi}\left[tan^{-1}\left(\frac{\omega - \Gamma_X}{\Gamma_W}\right) + \frac{\pi}{2}\right] \qquad (3)$$

here $\Gamma(\omega)$ in the extended Drude model is the frequency-dependent analogue of the Γ (frequency-independent) in the simple Drude model. Γ_L and Γ_H are the low-frequency and high-frequency damping constants respectively, Γ_X is the crossover-frequency from the low to high frequency region and Γ_W is the width of the crossover region.[5]

On a different note, the electric field at the surface of a NC extends to the space around it. Since NCs are well-separated from each other in a dilute solution, any near-field interaction between them can be negated, however, one can't completely rule out far-field interactions between NCs and, interactions between the NCs and the solvent molecules. These interactions change the overall dielectric environment around the NCs thereby modifying their optical response to the incident electromagnetic radiation. We employed Maxwell-Garnett effective medium approximation (MG-EMA), which neglects near-field interactions between adjacent NCs (electronically linked to each other) but takes into account the far-field interactions between NCs and interaction between the NCs and the solvent molecules. Using MG-EMA, the effective dielectric function ε_{eff} is given by,[14]

$$\frac{\varepsilon_{eff} - \varepsilon_H}{\varepsilon_{eff} + 2\varepsilon_H} = f_v \frac{\varepsilon_D - \varepsilon_H}{\varepsilon_D + 2\varepsilon_H} \qquad (4)$$

where ε_H is the dielectric medium of the solvent (2.26 for tetrachloroethylene), f_v is the volume fraction of NCs in the solution, and ε_D is the complex dielectric function of the material as described in equation (1). From equation (4), the absorbance of the solution can be approximated as 4π Im($\{\varepsilon_{eff}\}^{1/2}$) where Im ($\varepsilon_{eff}$) is the imaginary quotient of the effective dielectric function.

The MATLAB code developed by us combines

a) Equations (1)-(3) for simple Drude model considering ω_P, Γ and f_v as floating parameters.

b) Equations (1)-(4) for extended Drude model considering ω_P, Γ_L, Γ_H, Γ_X, Γ_w and f_v as floating parameters, to model the absorbance of our NC solution. Multiple fits were performed for each sample to ensure that the parameter values obtained after fitting do not deviate drastically between different fits.

ω_P can then be used to calculate the free electron density in the NCs. We note here that for calculating the electron density, we used an effective carrier mass of $0.22m_e$ for Zr:In_2O_3 NCs as suggested by Xu et. al.[15] and $0.39m_e$ for Sn:In_2O_3 and Sn,Zr:In_2O_3 NCs. Moreover, using the respective effective masses, one can optically derive DC mobility (μ_{opt}) of charge carriers in the material using equation 5.

$$\mu_{opt} = \frac{e}{m^*\Gamma} \qquad (5)$$

Once the mobility values are obtained, the DC electrical conductivity (σ) of the NC system can be calculated through equation (6),

$$\sigma = Ne\mu_{opt} \qquad (6)$$

Even though the above equations (5) and (6) are valid only for the simple Drude model (DC mobility has zero frequency and hence no frequency dependence), one can also employ it for the extended Drude model by using $\Gamma(0)$ from equation (3), i.e. damping constant at zero frequency. Average values of different parameters along with their standard deviation obtained from the extended Drude and simple Drude model have been tabulated in Table ST3 and Table ST4 respectively.

Table ST3: Parameters obtained through fits of optical extinction spectra by the extended Drude model. Electron density and optical electron mobility have been calculated from the fitting parameters using equations (1) and (5) in the main manuscript, respectively.

Composition	**ω_P (cm^{-1})**	**N (10^{20} cm^{-3})**	**Γ_L (cm^{-1})**	**Γ_H (cm^{-1})**	**Γ_X (cm^{-1})**	**Γ_W (cm^{-1})**	**μ_{opt} ($cm^2/V.s$)**
0% Doping	3880±2	0.37	389±59	841±23	1269±85	441±63	97.7±9.4
0.4% Zr	7290±1	1.31	872±3	536±3	2996±4	22.0±5	48.7±0.2
1.3% Zr	8535±1	1.79	725±4	1324±2	6021±33	48±24	58.4±0.3
1.6% Zr	8970±4	1.98	1196±5	617±6	3274±14	326±11	35.9±0.1
2.3% Zr	9572±2	2.25	1035±23	682±22	3393±20	162±29	41.2±0.9
0.6% Sn	6027±4	1.58	1109±1	767±7	3780±20	62±10	21.6±0.1
2.8% Sn	11719±5	5.98	1718±200	853±85	3926±231	808±336	14.5±1.4
4.1% Sn	13626±3	8.08	1437±34	611±83	5318±117	448±129	16.9±0.1
7.5% Sn	16624±1	12.0	1247±9	611±29	7261±27	202±46	19.3±0.1
1.9% Sn-0.9% Zr	10778±1	5.06	661±9	2319±164	7436±49	135±55	35.6±0.3
0.9% Sn-0.4% Zr	8876±2	3.43	745±7	886±3	2892±9	55±8	32.1±0.3
4.5% Sn-0.8% Zr	14156±2	8.72	579±14	1060±8	4306±4	98±19	41.1±0.8
7.5% Sn-1.0% Zr	16240±3	11.5	856±14	1103±11	5329±18	136±12	27.9±0.4

Table ST4: Parameters obtained through the fitting of the optical extinction spectra using the simple Drude model. Electron density and optical electron mobilities, DC electrical conductivity were obtained by substituting the fitting parameters in equation (1) and equation (5) and equation (6), respectively.

Composition	**ω_P (cm^{-1})**	**N (10^{20} cm^{-3})**	**Γ (cm^{-1})**	**μ_{opt} ($cm^2/V.s$)**	**σ (S/cm)**
0% Doping	3879	0.37	680	62.4	369.4
0.4% Zr	7260	1.29	790	53.7	1108.4
1.3% Zr	8516	1.78	752	56.4	1606.3
1.6% Zr	8998	1.99	932	45.5	1448.7
2.3% Zr	9597	2.26	905	46.9	1695.9
0.6% Sn	6020	1.58	1074	22.3	563.7
2.8% Sn	11745	6.0	1219	19.6	1881.6
4.1% Sn	13613	8.06	1221	19.6	2527.6
7.5% Sn	16613	12.0	1198	19.9	3820.8
1.9% Sn-0.9% Zr	10780	5.06	686	34.9	2825.5
0.9% Sn-0.4% Zr	8865	3.42	860	27.8	1521.2
4.5% Sn-0.8% Zr	14185	8.76	960	24.8	3475.9
7.5% Sn-1.0% Zr	16228	11.5	1022	23.4	4305.6

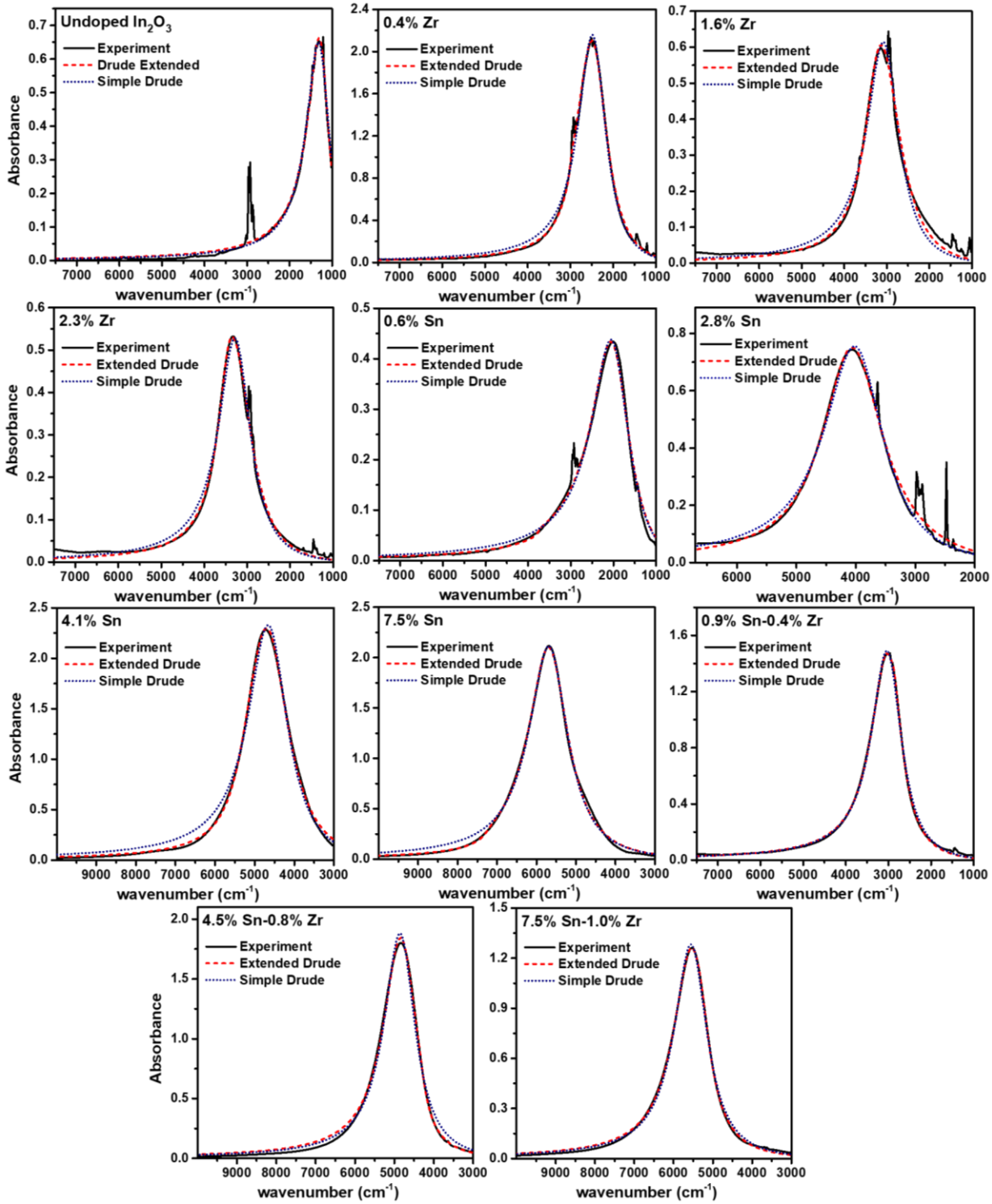

Figure S9: Simple Drude and extended Drude model fits to the optical extinction spectra of different Zr:In_2O_3, Sn:In_2O_3 and Sn,Zr:In_2O_3 NCs.

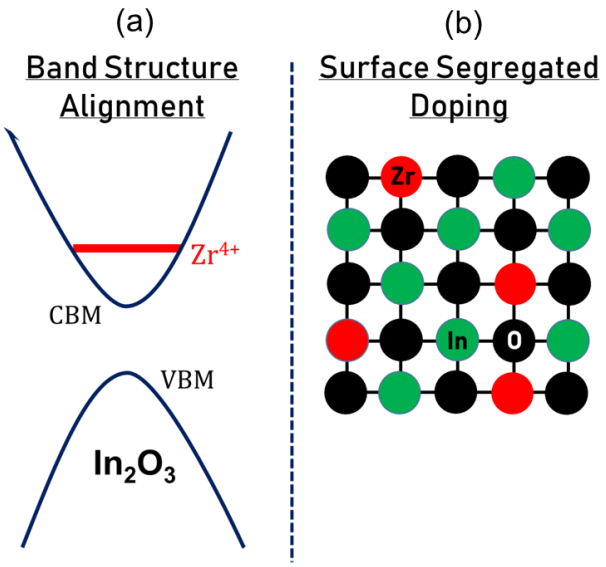

Figure S10: A schematic description of the factors responsible for high LSPR quality factors observed from Zr-doped In_2O_3 NCs (a) A position of the Zr level deep in the conduction band of In_2O_3 leading towards lower effective electron mass (high LSPR energy) and low electron scattering (low LSPR FWHM) (b) Surface segregated doping of Zr responsible for minimized change in electrostatic potential experienced by the electrons in the NC leading to low electron scattering (low LSPR FWHM) and consecutively, high LSPR quality factors.

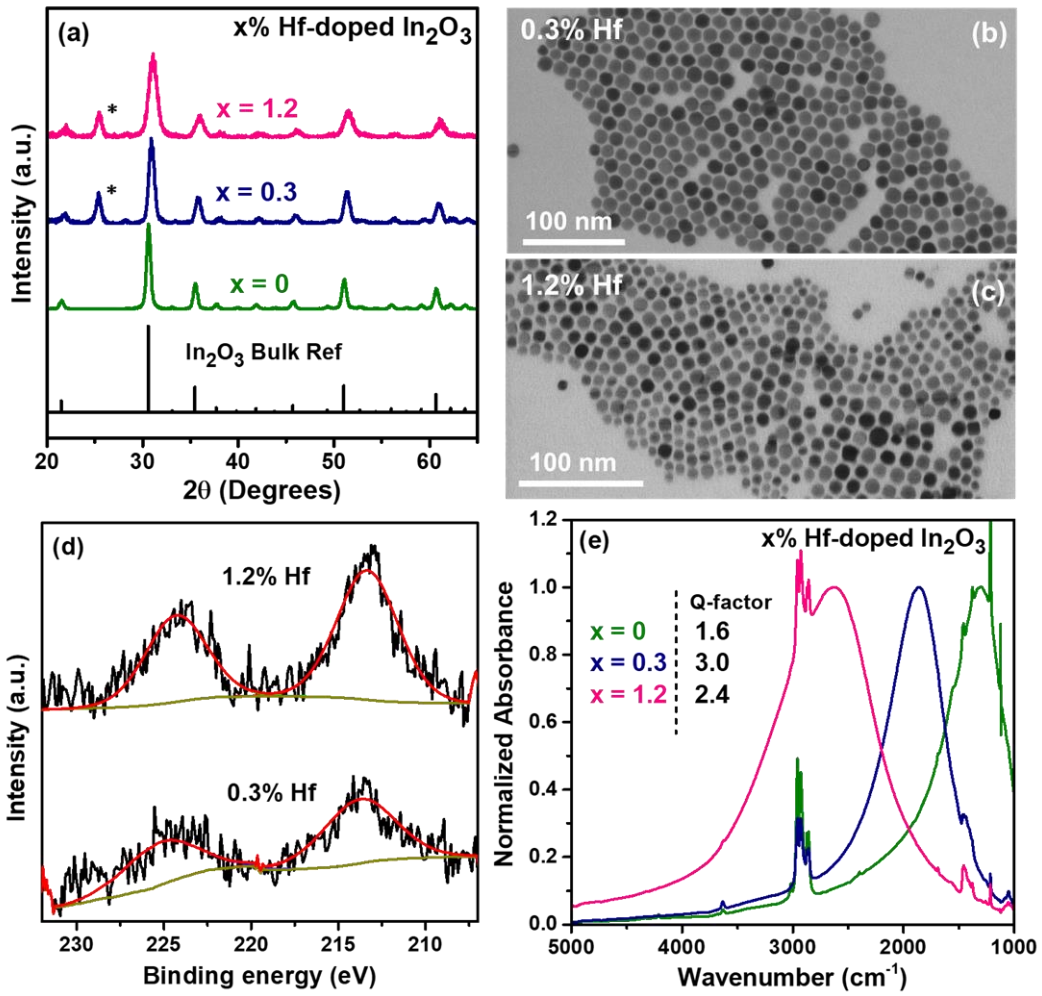

Figure S11: Hf-doped In_2O_3 (Hf:In_2O_3) NCs as an example of the dopant selection strategy**.** Since both the chemical and physical properties of Hf and Zr are very similar due to lanthanide contraction, Hf doping in the In_2O_3 lattice is also expected to generate LSPR similar to Zr, as shown in the main manuscript. (a) Comparison of XRD patterns of Hf:In_2O_3 NCs with undoped In_2O_3 NCs and bulk reference (JCPDS 88-2160) shows retention of the cubic bixbyite phase, absence of any impurity and a gradual shift in diffraction peak with increase in Hf doping percentage. Peaks marked with an asterisk (*) are due to the substrate. (b-c) STEM micrographs of Hf:In_2O_3 NCs (d) XPS spectra of Hf 3d for Hf:In_2O_3 NCs showing binding energy peaks corresponding to +4 oxidation state of Hf and theoretical peak fit depicting the presence of single oxidation state. (e) Optical extinction spectra of Hf:In_2O_3 NCs showing narrow LSPR bands increasing in energy with an increase in the Hf doping concentration.

References:

1. Jansons, A. W.; Hutchison, J. E., Continuous Growth of Metal Oxide Nanocrystals: Enhanced Control of Nanocrystal Size and Radial Dopant Distribution. *ACS Nano* **2016,** *10*, 6942-6951.
2. Ye, X.; Fei, J.; Diroll, B. T.; Paik, T.; Murray, C. B., Expanding the Spectral Tunability of Plasmonic Resonances in Doped Metal-Oxide Nanocrystals through Cooperative Cation–Anion Codoping. *J. Am. Chem. Soc.* **2014,** *136*, 11680-11686.
3. Gordon, T. R.; Paik, T.; Klein, D. R.; Naik, G. V.; Caglayan, H.; Boltasseva, A.; Murray, C. B., Shape-Dependent Plasmonic Response and Directed Self-Assembly in a New Semiconductor Building Block, Indium-Doped Cadmium Oxide (ICO). *Nano Lett.* **2013,** *13*, 2857-2863.
4. Tandon, B.; Yadav, A.; Khurana, D.; Reddy, P.; Santra, P. K.; Nag, A., Size-Induced Enhancement of Carrier Density, LSPR Quality Factor, and Carrier Mobility in Cr–Sn Doped In_2O_3 Nanocrystals. *Chem. Mater.* **2017,** *29*, 9360-9368.
5. Lounis, S. D.; Runnerstrom, E. L.; Bergerud, A.; Nordlund, D.; Milliron, D. J., Influence of Dopant Distribution on the Plasmonic Properties of Indium Tin Oxide Nanocrystals. *J. Am. Chem. Soc.* **2014,** *136*, 7110-7116.
6. Runnerstrom, E. L.; Bergerud, A.; Agrawal, A.; Johns, R. W.; Dahlman, C. J.; Singh, A.; Selbach, S. M.; Milliron, D. J., Defect Engineering in Plasmonic Metal Oxide Nanocrystals. *Nano Lett.* **2016,** *16*, 3390-3398.
7. Johns, R. W.; Bechtel, H. A.; Runnerstrom, E. L.; Agrawal, A.; Lounis, S. D.; Milliron, D. J., Direct Observation of Narrow Mid-Infrared Plasmon Linewidths of Single Metal Oxide Nanocrystals. *Nat. Commun.* **2016,** *7*, 11583.
8. Luther, J. M.; Jain, P. K.; Ewers, T.; Alivisatos, A. P., Localized surface plasmon resonances arising from free carriers in doped quantum dots. *Nat. Mater.* **2011,** *10*, 361-366.
9. Manthiram, K.; Alivisatos, A. P., Tunable Localized Surface Plasmon Resonances in Tungsten Oxide Nanocrystals. *J. Am. Chem. Soc.* **2012,** *134*, 3995-3998.
10. Della Gaspera, E.; Bersani, M.; Cittadini, M.; Guglielmi, M.; Pagani, D.; Noriega, R.; Mehra, S.; Salleo, A.; Martucci, A., Low-Temperature Processed Ga-Doped ZnO Coatings from Colloidal Inks. *J. Am. Chem. Soc.* **2013,** *135*, 3439-3448.
11. De Trizio, L.; Buonsanti, R.; Schimpf, A. M.; Llordes, A.; Gamelin, D. R.; Simonutti, R.; Milliron, D. J., Nb-Doped Colloidal TiO_2 Nanocrystals with Tunable Infrared Absorption. *Chem. Mater.* **2013,** *25*, 3383-3390.
12. Mendelsberg, R. J.; Garcia, G.; Li, H.; Manna, L.; Milliron, D. J., Understanding the Plasmon Resonance in Ensembles of Degenerately Doped Semiconductor Nanocrystals. *J. Phys. Chem. C* **2012,** *116*, 12226-12231.
13. Lounis, S. D.; Runnerstrom, E. L.; Llordés, A.; Milliron, D. J., Defect Chemistry and Plasmon Physics of Colloidal Metal Oxide Nanocrystals. *J. Phys. Chem. Lett.* **2014,** *5*, 1564-1574.
14. Ghosh, S. K.; Pal, T., Interparticle Coupling Effect on the Surface Plasmon Resonance of Gold Nanoparticles: From Theory to Applications. *Chem. Rev.* **2007,** *107*, 4797-4862.
15. Xu, J.; Liu, J. B.; Liu, B. X.; Li, S. N.; Wei, S. H.; Huang, B., Design of n-Type Transparent Conducting Oxides: The Case of Transition Metal Doping in In_2O_3. *Adv. Electron. Mater.* **2018,** *4*, 1700553.